

Design and Fabrication of RGO/WO₃ as A Novel Photoanode For High Efficient Dye-Sensitized Solar Cells

K. Ramesh

Bharathiar University

B Gnanavel (✉ gnanavelphd@gmail.com)

Chikkaiah Naicker College <https://orcid.org/0000-0003-0646-1599>

Original Research

Keywords: WO₃, Reduced graphene oxide, Photoanode, Photo-conversion efficiency, DSSCs.

Posted Date: February 9th, 2021

DOI: <https://doi.org/10.21203/rs.3.rs-166108/v1>

License:  This work is licensed under a Creative Commons Attribution 4.0 International License.

[Read Full License](#)

Abstract

The hydrothermal approach for photovoltaic applications introduces an easy and scalable synthesis of RGO/WO₃ nanocomposites. Some advanced techniques such as X-ray diffraction, scanning electron microscopy, transmission electron microscopy and Raman spectroscopy showed that high-quality RGO/WO₃ nanocomposites contained single crystal WO₃ nanoparticles in the characterization of RGO/WO₃ nanocomposites. Due to its charge transport and light-scattering properties, the RGO/WO₃ photoanode with DSSC greatly improved the cell efficiency. A power conversion efficiency of 7.9 % was demonstrated by the RGO/WO₃ DSSC, which is better than that of the bare WO₃ (4.1 %) and industrial Pt (6.5 percent) electrolytes. Our findings indicate that the electrochemical efficiency of the RGO/WO₃ electrode shows a higher charge transfer and series cell resistance of 64.9 and 6.88 cm², respectively) than the RGO electrode and is equivalent to the Pt electrode.

1. Introduction

Water and energy are the keys of daily life and have the crucial need for economic prosperity. There are numerous applications that are now increasingly dependent on fossil fuels in developed economies. Only by the extraction of cheap fossil fuels [1] has global growing population, new amenities and mechanised farming been largely created. The biggest obstacle faced by all communities in this country [2] would be ensuring safe and potential energy resources. Photovoltaic cells are among the most promising sources of renewable energy supply due to its low cost, and extensive investigations have been carried to improve their performance in power conversion [3]. Thanks to its basic structure, Dye sensitised solar cells (DSSC) have been extensively studied as a next century solar cell. And the low cost of production. One of the key components in the photo photosensitizer in DSSCs that can show strong efficiency gains in the conversion of electricity from solar energy [4, 5]. Dye sensitization was shown to cause visible light photo catalytic activity on the layer of wide band gap semiconductors such as TiO₂, which itself is ineffective in visible light[7–11] as a helpful tool. DSSCs have many benefits, i.e. they can be built into compact panels, use low-cost products for immune responses, are easy to produce, and requires minimal processing temperatures. Due to its behaviour in ultraviolet region, narrow band gap (2.4–2.8 eV), deeper conduction bands (~ 3.1 eV), superior physicochemical properties and high stability, tungsten oxide (WO₃), an n-type semiconductor, has garnered great attention to its usefulness in catalysts [12–14].

Several researchers have achieved an improvement in the photocatalytic activity and photovoltaic action of WO₃ by adopting methods such as noble metal deposition [8] and composite formation [15]. Outstanding graphene and rGO properties have attracted considerable interest, like high surface area, high electrical conductivity (106 S cm⁻¹), carrier mobility (200000 cm⁻² V⁻¹ S⁻¹) and effective aggregation and transfer of electrons (e) [16]. Thus, by combining the specifications of WO₃ and RGO, a material with excellent functional value could be given. Very few papers on graphene and RGO-WO₃ composites for the implementation of PEC[17, 18] are accessible and require repetitive procedures. Yet, occasional news accounts rely on using tungsten oxides in DSSC as counter electrodes. In this work,

reduced graphene oxide (RGO)-supported tungsten dioxide (WO_3) was composed and tested as photoanodes for use in the DSSC method and provides a high PCE and strong electrocatalytic activity compared to the untreated WO_3 .

2. Experimental Procedure

2.1. *Synthesis of WO_3 and RGO/ WO_3 nanocomposites*

Centered on the modified Hummer's strategy, GO was synthesised. The one-step hydrothermal methodology was proposed for the processing of RGO- WO_3 composites. First, with the help of an ultrasonicator, the graphene oxide as prepared was distributed in DI water, creating a stable suspension with a volume of 50 mg mL^{-1} . A sufficient quantity of $\text{Na}_2\text{WO}_4 \cdot 2\text{H}_2\text{O}$ was then diluted in 50 mL of DI water. In the above solution, varying concentrations of (0.25, 0.5 and 1 percent wt) were then extracted. After that, in the 10 mL mixture with constant stirring, 35% HCl was then slowly applied to 5 mL. The suspension was moved to an autoclave of 100 mL Teflon-lined stainless to undergo a warming phase at 140°C for 12 h. The sample was extracted and washed repeatedly with ethanol and DI water after getting cold naturally until being dried by the vacuum frozen drier. The same process was used to create a pure WO_3 sample where $\text{Na}_2\text{WO}_4 \cdot 2\text{H}_2\text{O}$ was dissolved by DI water instead of GO suspension. The three samples were called WGO0.25, WGO0.5 and WGO1, respectively, with varying RGO dosages.

3. Results And Discussion

3.1. Powder X-ray diffraction (XRD) analysis

The powder XRD sequence of composites of RGO, WO_3 , and WO_3/ZnO as seen in Fig. 1. A sharp crest at $2\theta = 26.0^\circ$ referring to the crystalline plane (002) belonging to graphene oxide is in bare RGO. The pure WO_3 XRD pattern adopted the regular XRD pattern of m- WO_3 well (PDF NO: 01-083-0951). The sharp peaks displayed the strong crystallinity and no other peak was discovered indicating the high WO_3 purity obtained. The XRD patterns were very similar to WO_3 for RGO- WO_3 composites, but in the XRD pattern of WGO1, a large peak centred at around $25\text{--}30$ was observed. In agreement with the (002) planes occurring from the graphic graphene sheet, this broad peak was. More importantly, compared to the XRD pattern of GO, the distinctive peak of GO at around 10° was not noted in the three RGO- WO_3 composites, authenticating that GO had been significantly lowered to RGO.

3.2. Morphological analysis

SEM images of RGO, WO_3 , and RGO/ WO_3 composite samples are shown in Fig. 2. The bare sheet-exposed RGO (Fig. 2a) and WO_3 show great, precise morphology with certain exterior conglomerations (Fig. 2). In the composite sample, the WO_3 nanoparticles are coated on the RGO surface (Fig. 2c). In the TEM image, the freckle type with cleverer framework sheet of RGO was obviously found (Fig. 2d). The

less coagulated specific WO_3 nanoparticles (Fig. 2e) are found and distributed evenly on the exterior of the RGO sheets (Fig. 2f). To find out the RGO in WO_3 , the elemental mapping of the WGO1 sample was evaluated and the associated photographs are shown in Fig. 2. (g-i).

3.3. Raman spectra analysis

As shown in Fig. 3, the Raman spectral analysis was performed to examine the ability to interact among both RGO and WO_3 . There were two peaks in the Raman spectra of bare RGO: the D-band peak at 1387 cm^{-1} and the G-band peak at 1556 cm^{-1} wavenumber. The peaks acquired in the Raman spectrum confirm the WO_3 crystallographic phase and are well suited to literature reports [19]. At 715 and 826 cm^{-1} , the W-O-W bending mode was ascertained in the WO_3 system. In the RGO/ WO_3 matrix, the WO_3 peak magnitudes are reduced, that may be due to a reduction in the shape of WO_3 particles on RGO. It is important to note that the G band was rise from 1556 to 1570 cm^{-1} contrasted to RGO in the RGO- WO_3 nanostructures, confirming the synthetic doping of carbon materials in WO_3 [19]. Rather than mixing equal RGO and WO_3 , this chemical doping indicates the creation of an authentic composite.

3.4. Optical studies

The UV-vis DRS spectrum of WO_3 and three composite materials of RGO/ WO_3 are shown in Fig. 4 (a). Meanwhile, Bare WO_3 showed light absorption in the visible range with the on uptake at 460 nm . By contrast, as reported earlier in other graphene-based composite materials, the RGO/ WO_3 composite exhibited largely increased absorption in the visible light range ($480\text{--}550\text{ nm}$) resulting from the emergence of RGO. Two possible reasons might be attributed to this improved visible light response: (1) RGO's background light absorption in the visible light region, and (2) WO_3 's improved ground electrical potential regarding the possible electronic transition between both the n orbit of the reactive oxygen $\pi \rightarrow \pi^*$ of RGO and $n \rightarrow \pi^*$. The band gaps were computed using the modified function of Kubelka-Munk as a graph in the indented Fig. 4 4 (b). For WO_3 , WGO0.25, WGO0.5 and WGO1, respectively, the estimated band gap energies are 2.58 , 2.49 , 2.31 and 2.25 eV . The room temperature PL of the samples with an excitation wavelength of 325 nm is shown in Fig. 5. In the visible light region ($460\text{--}550\text{ nm}$), all the samples show a broad emission that is in excellent accordance with the UV results. The RGO/ WO_3 nanocomposites can effectively affect electron-hole pair replication and wholeheartedly support the flow of energy from the WO_3 band gap to the rGO electron density. Reduced PL emissions could considerably enhance the solar performance of the device by preventing the electron-hole charge recombination.

3.5. Textural and elemental composition analysis

Figure 6 (a&b) shows the BET surface area of the pure WO_3 and RGO/ WO_3 (WGO1) nanocomposites and the corresponding BJH pore size. Strangely, both samples showed isotherm models of type IV, attributed to the formation of mesoporous materials with a pressure range of 0.1 to 0.9 [22, 23]. 39.96 and $78.67\text{ m}^2/\text{g}$ were found to be specific surface areas of pure WO_3 and RGO/ WO_3 (WGO1), respectively. While, 12.53 and 21.45 nm are the corresponding pore sizes, respectively. The increased efficiency of the

RGO/WO₃ (WGO1) nanocomposite is confirmed by this outcome and the small rise in pore size may be attributed to the addition of a larger number of layers of graphene.

3.6. XPS analysis

The survey spectrum with W 4f, O 1s and C 1s core level spectra are shown in Fig. 7(a–d). The W 4f core level corresponds to binding energies 35.1 and 37.9 eV for W 4f₊ and W 4f_{5/2} respectively. The O 1s spectrum (Fig. 7(c)) shows two peaks positioned at 530.4 and 532.5 eV. The former peak with maximum intensity is due to the W = O bonding modes of WO₃ corresponding to oxygen atoms O₂ in the lattice. Further, the C 1s shows two peaks at 284.1 and 287.5 eV as seen in Fig. 7(d), which correspond to the binding states of the C = C and C–O–W bonds in the nanocomposite samples.

3.7. Photovoltaic studies

Figure 8a) displays the schematic description of the fabricated DSSC. The utility of DSSCs from various photoanodes is seen in Fig. 8b). Dye sensitized solar cells prepared using RGO/WO₃ (WGO1) nanocomposites as photoanode shows the power conversion efficiency (η) of 7.9 %, which is huge than compared to DSSC with WO₃ (4.1%). With more surface area for adsorption capacity, the WO₃ nanostructures result in an improvement in electron-hole pair production and thus short-circuit density. The photon-to-current conversion efficiency (IPCE) incident of dye sensitised solar cells equipped using all the photoanodes is shown in Fig. 8c). The finding provides evidence that dye sensitised solar cells designed using RGO/WO₃ (WGO1) have more red-shifted effective photon-to-current reactions compared to bare WO₃, which means that the spectral absorption spectrum is essentially expanded. In comparison, RGO/WO₃ (WGO1) has a strong IPCE of 71 % relative to the bare WO₃ (32 %). In order to understand the use of functional system implementations, stability checks were also carried out regularly over a 60 day duration (Fig. 8d). At the end of the 60-day test, a marginal decline in PCE was observed. This is primarily due to dye molecule inactivation and degradation. In attempt to comprehend the charge kinetic mechanism, EIS was done. The Nyquist plot of the electrode samples as seen in Fig. 9a.) The charge transfer resistance (R_{ct}) was measured (Table 2) as per the configured corresponding circuit (inset of Fig. 9(a)) from the Nyquist plot of the electrodes. The R_{ct} value of the RGO/WO₃ (WGO1) photoanode indicates a lower value of 18.5 Ω cm² relative to the bare WO₃ (112.5 Ω cm²), which is responsible for the increase of the captured solar light in charge transport. The big decrease in the R_{ct} value of photoanode composites within RGO/WO₃ (WGO1) is due to the effective isolation of photo-generated electron-hole pairs and the fast transition of interaction charges. Figure 9b) displays the potential DSSCs' photovoltaic process. The RGO/WO₃ composite's high solar efficiency is due to the improved ion transport and light diffusion characteristics that can constrain the light beam to the electrolyte/electrode and reduce the intercellular resistance, thus enhancing the productivity of the cell. The RGO integration will have the high surface area and conducting nature can enhance the cells' light harvesting efficiency by eliminating the recombination rate and the performance of DSSCs photo-conversion.

4. Conclusions

In brief, to synthesise RGO/WO₃ composites with better PCE and long term sustainability, a simple one-step hydrothermal methodology was designed. Both three RGO/WO₃ composites displayed substantially improved light harvesting capability with outstanding electrocatalytics relative to pure WO₃. Of the three RGO/WO₃ composites, the RGO/WO₃ (WG01) composite showed excellent PCE, rendering it a more successful candidate. Current research offers a low-cost and convenient method of producing RGO/WO₃ composites, and it is possible to consider such RGO/WO₃ composites as a potential photoanode for applications of dye sensitised solar cells.

References

1. M. Grätzel, J. Photochem, Photobiol. A 164 (2004) 3-14.
2. H.Y. Kim, M.W. Lee, D.H. Song, H.J. Yoon, J.S. Suh, J. Appl. Phys. 121 (2017) 43103.
3. F. Bella, C. Gerbaldi, C. Barolo, M. Grätzel, Chem. Soc. Rev. 44 (2015) 3431-3473.
4. B. Oregan, M. Grätzel, Nature 353 (1991) 737-740.
5. O.A. Blackburn, B.J. Coe, V. Hahn, M. Helliwell, J. Raffery, Y.T. Ta, L.M. Peter, H. Wang, J.A. Anta, E. Guillen, Dye Pigment. 92 (2011) 766–777
6. Mohamed AM, Shaban SA, El Sayed HA, Alanadouli BE, Allam NK. Int J Hydrogen Energy. 41 (2016) :866-872.
7. Kumar SG, Rao KSRK. Appl. Surf. Sci. 391 (2017) 124-48.
8. Bamwenda GR, Arakawa H., Appl Catal A General. 210 (2001) 181-191.
9. Zhou M, Yan J, Cui P. Mater. Lett. 89 (2012) 258-261.
10. Khan I, Abdalla A, Qurashi A. Int J Hydrogen Energy. 42 (2017) 3431-3439.
11. Gao H, Zhang P, Hu J, Pan J, Fan J, Shao G. Appl Surf Sci. 391 (2017) 211-217
12. Lin J, Hu P, Zhang Y, Fan M, He Z, Ngaw CK, et al. RSC Adv. 3 (2013) 9330-9336.
13. Ng YH, Iwase A, Bell NJ, Kudo A, Amal R. Catal Today. 164 (2011) 353-357.
14. Wu H, Xu M, Da P, Li W, Jia D, Zheng G. Phys Chem Chem Phys. 15 (2013) 16138-16142.
15. Bamwenda GR, Arakawa H. Mater Lett. 89 (2019) 258-261.
16. F. Xu, L. Sun, Ener. Environ. Sci. 4 (2011) 818.
17. M. H. Habibi, M. Mikhak, M. Zendehtdel , M. Habibi, Int. J. Electrochem. Sci. 7 (2012) 6787.
18. G. Zeng, K. Nian, K. Lee, Diamond Relat. Mater. 19 (2010) 1457.
19. D. Wei, H.E. Unalan, D. Han, Q. Zhang, L. Niu, G. Amaratunga, T. Ryhanen, Nanotech. 19 (2008) 4424006.
20. J. Liu, A.G. Rinzler, H. Dai, J.H. Hafner, R.K. Bradley, P.J. Boul, A. Lu, T. Iverson, Shelimov, C.B. Huffman, F. Rodriguez- Macias, Y.S. Shon, T.R. Lee, D.T. Colbert, R.E. Smalley, Science. 280 (1998) 1253.

21. F Liu, XB Zhang, D Haussler, W Jager, GF Yi, JP Cheng, XY Tao, ZQ Luo, S.M. Zhou, J. Mater. Sci. 41 (2006) 4523
22. J. Yu, T. Ma, S. Liu, Phys. Chem. Chem. Phys. 13 (2011) 3491–3501.
23. S. Aliyu, H. Abdullah, Z. Abbas, Int. J.

Tables

Due to technical limitations, table 1,2 is only available as a download in the Supplemental Files section.

Figures

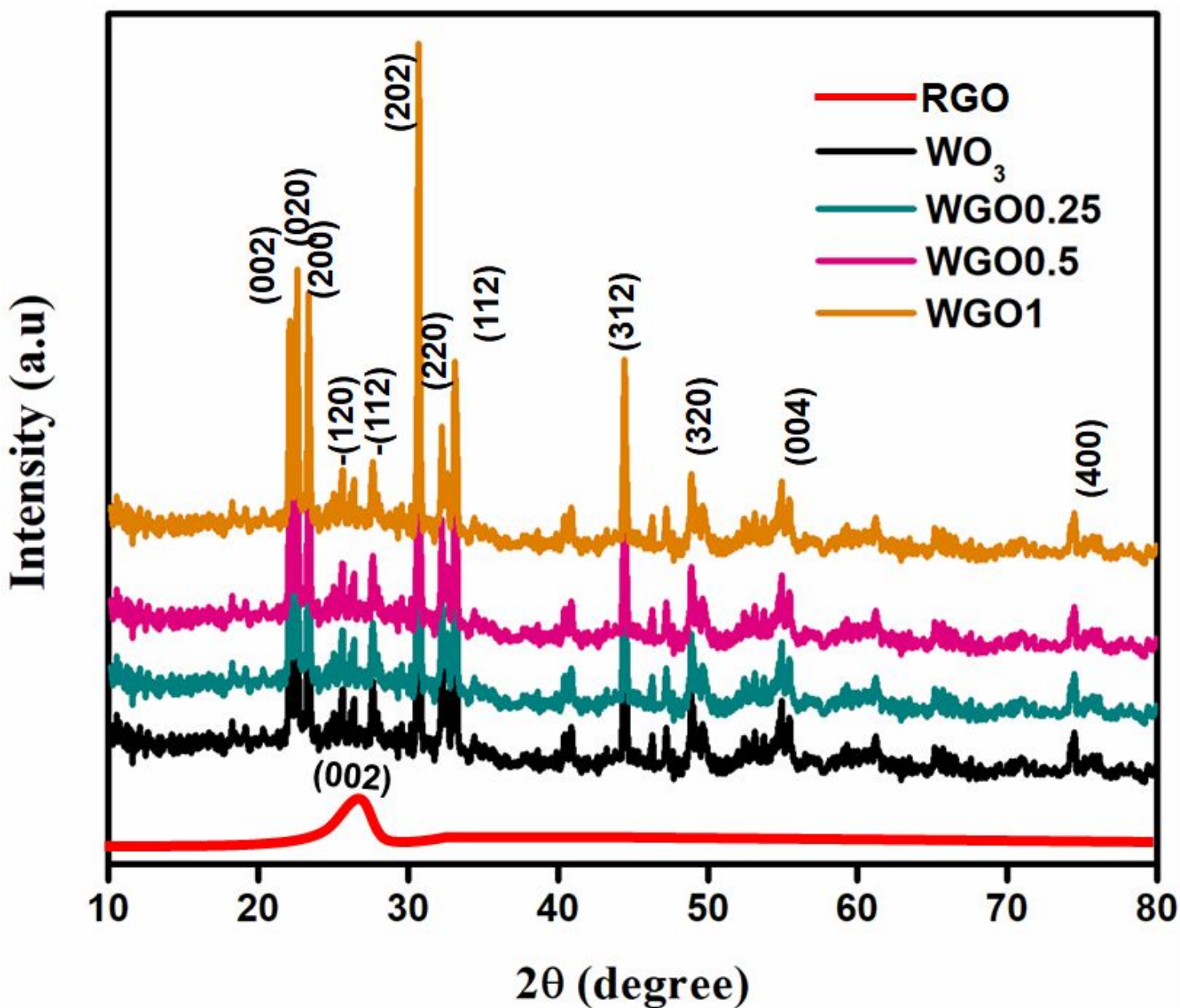


Figure 1

Powder X-ray diffraction pattern of the electrode samples

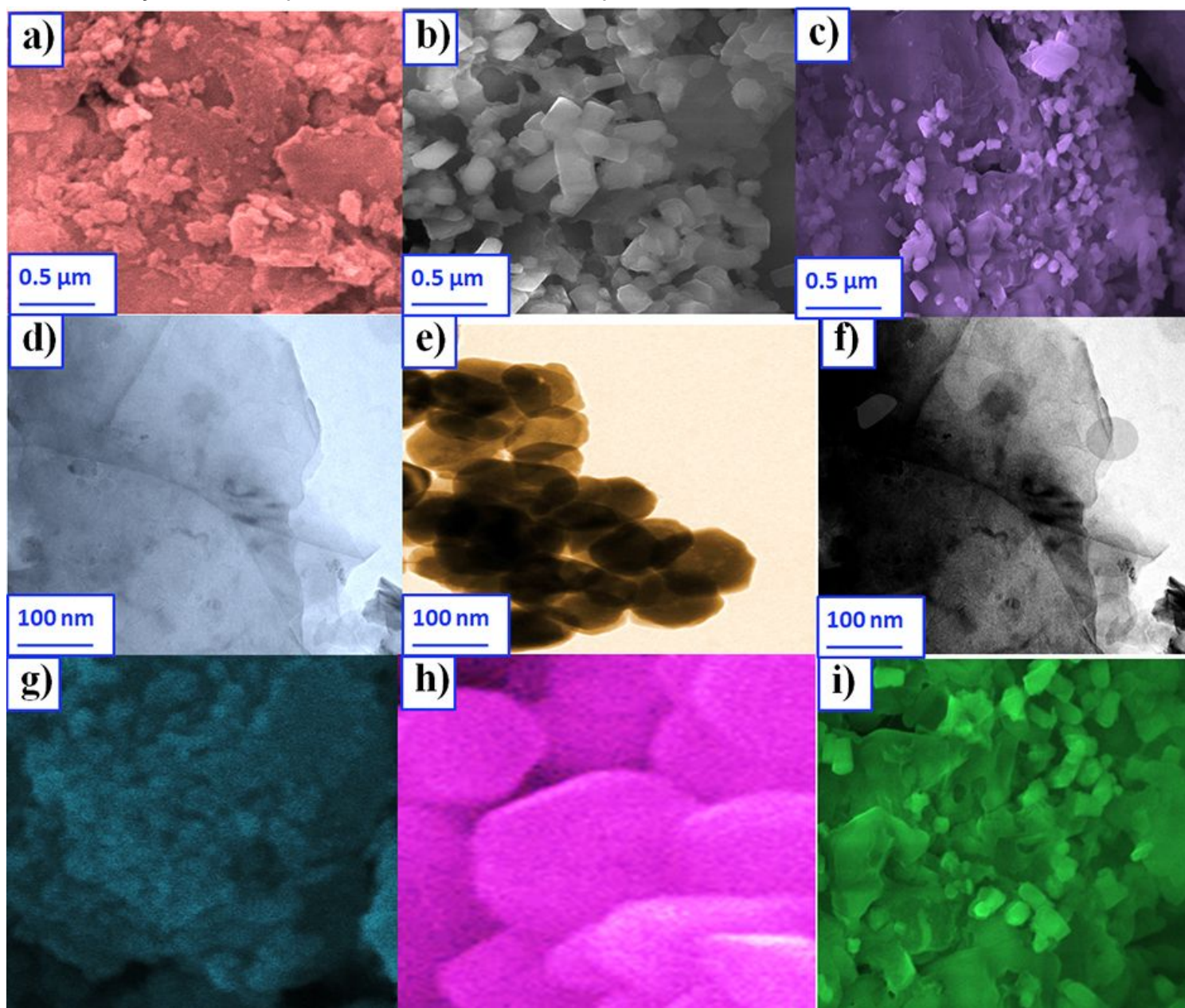


Figure 2

SEM images of (a) RGO; (b) WO₃; (c) WGO1; TEM images of (d) RGO; (e) WO₃; (f) WGO1; Elemental mapping image of (g) C, (h) W and (i) O

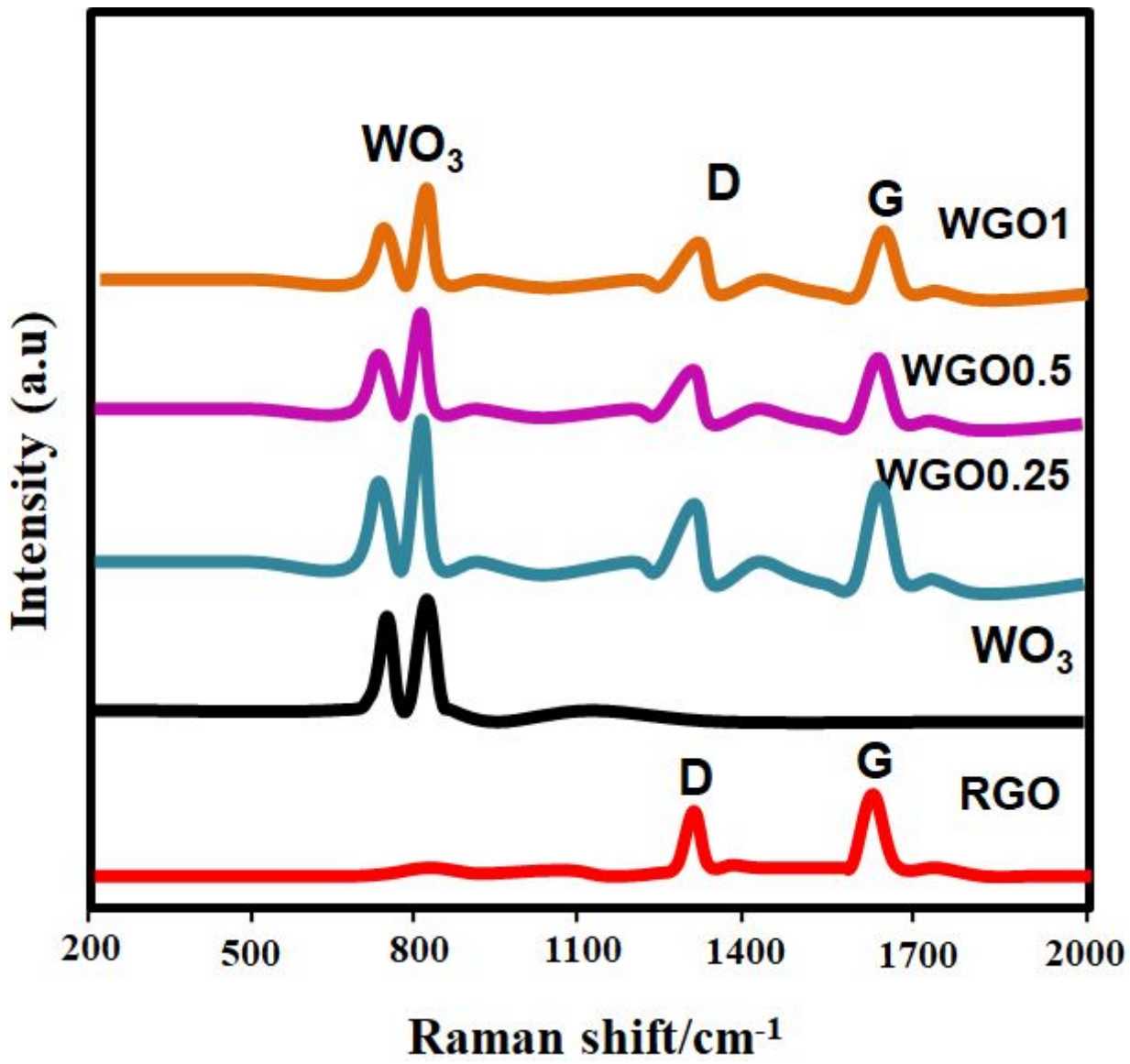


Figure 3

Raman spectra of the electrode samples

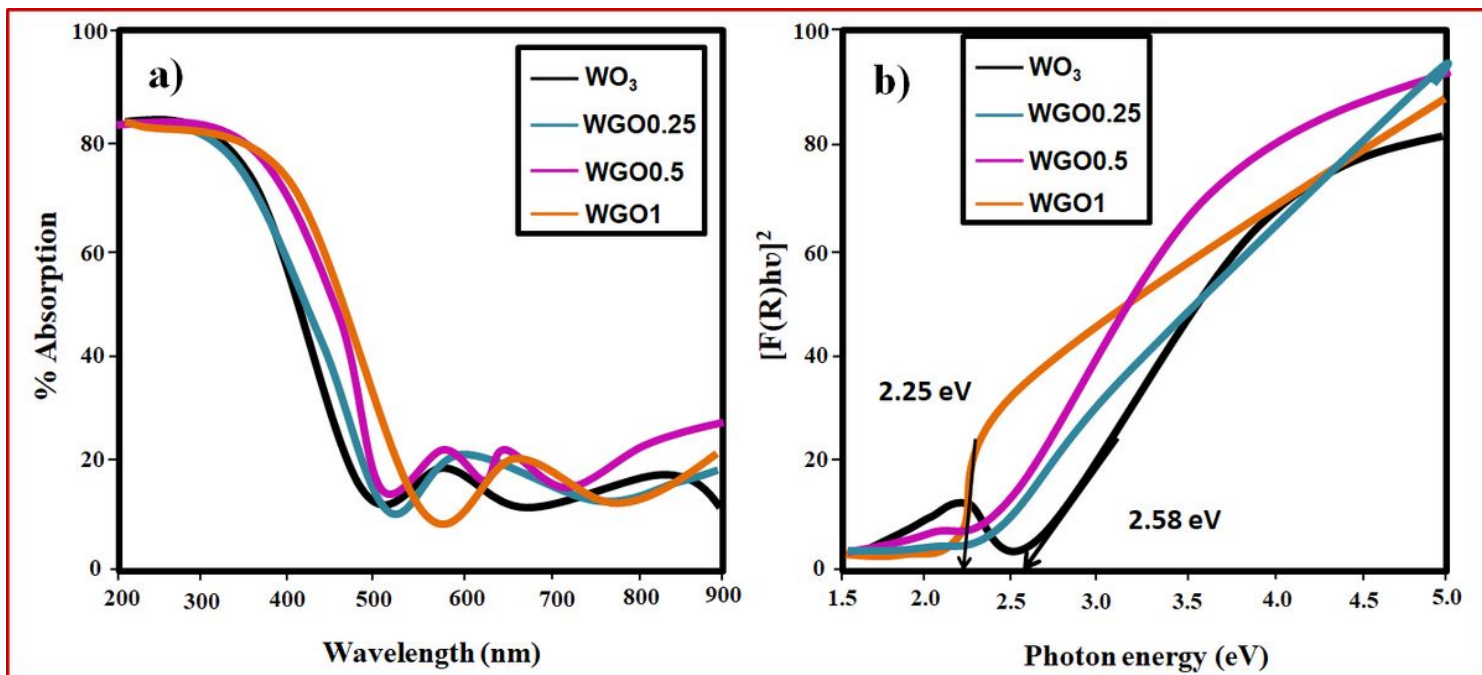


Figure 4

(a) UV-Vis absorption spectra of the electrode samples; (b) band gap plot

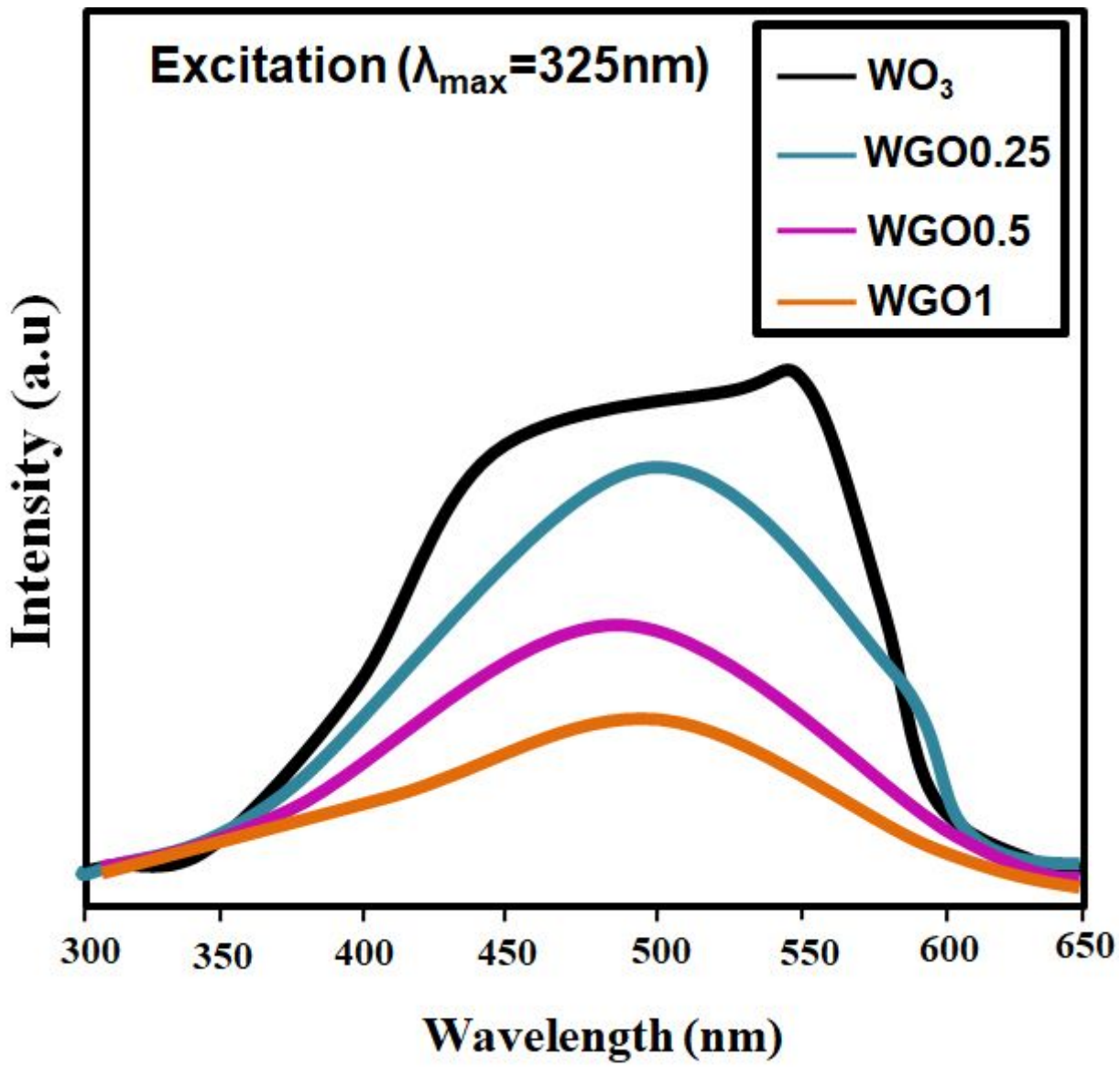


Figure 5

Photoluminescence spectra of the electrode samples

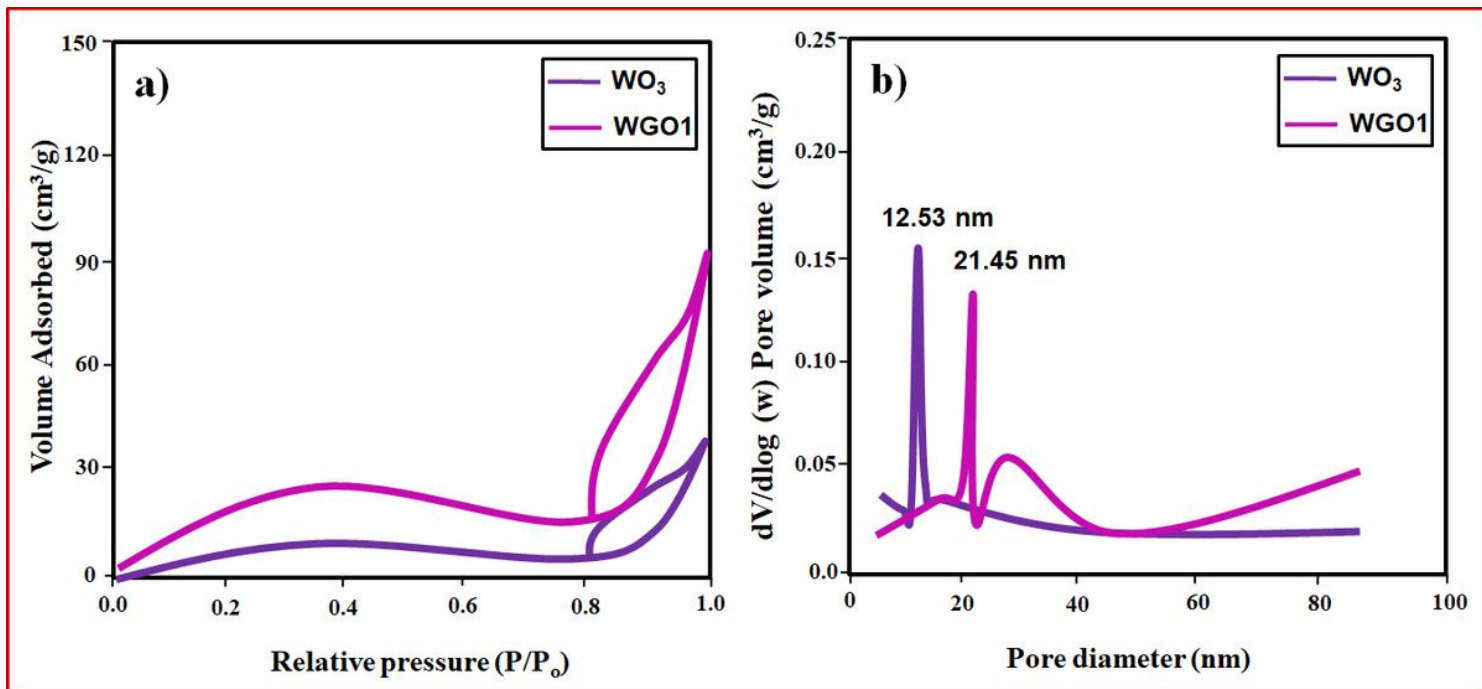


Figure 6

(a) N₂ adsorption and desorption analysis WO₃ and WGO1 samples (b) corresponding pore size distribution

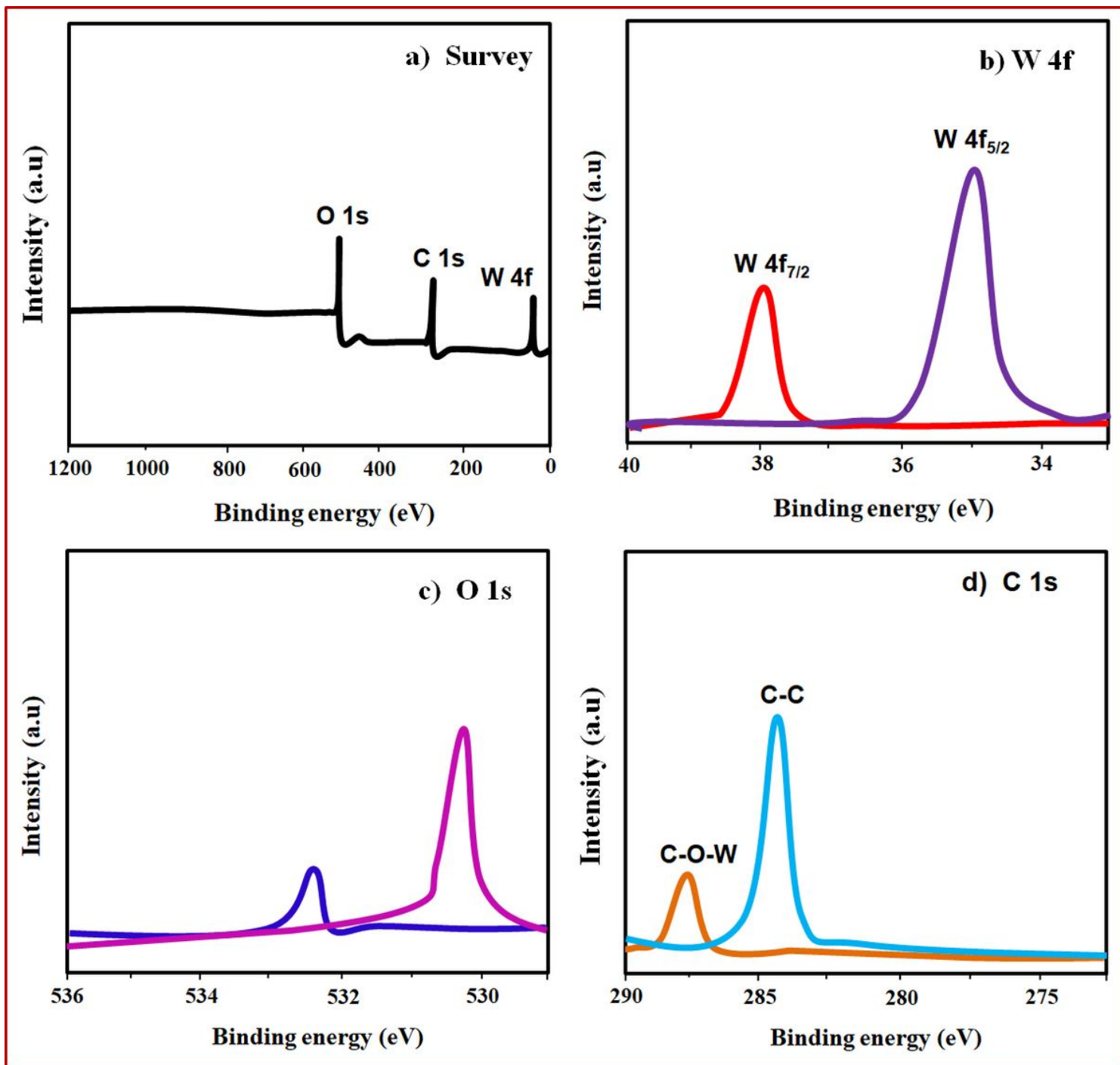


Figure 7

XPS spectra of W_{0.3}/RGO (WG01) sample (a) survey; (b) W 4f; (c) O 1s; (d) C 1s.

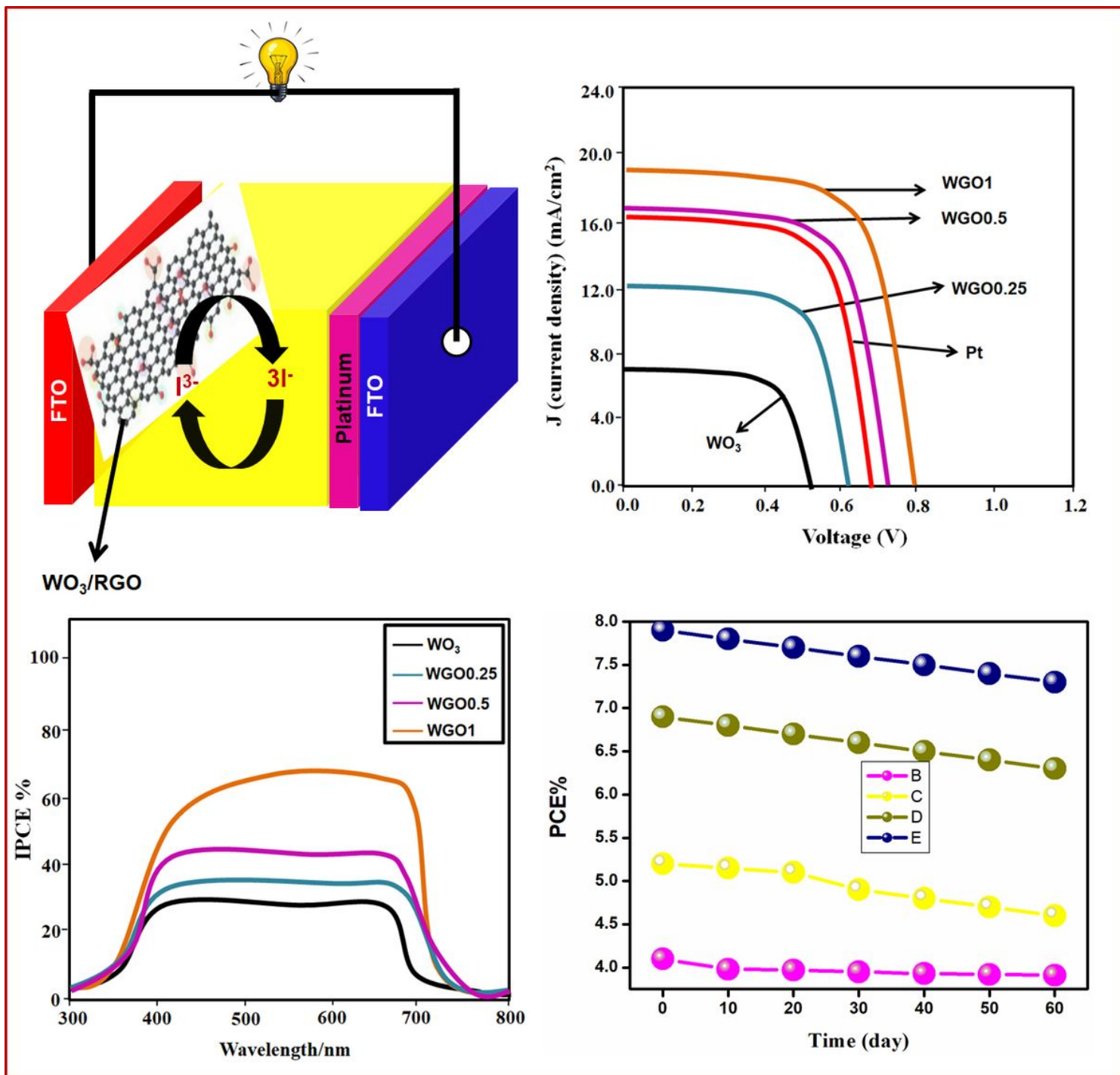


Figure 8

(a) Schematic representation of the sandwich type solar cell device; (b) J-V characteristics of all the photoelectrodes; (c) IPCE spectra; (d) stability test

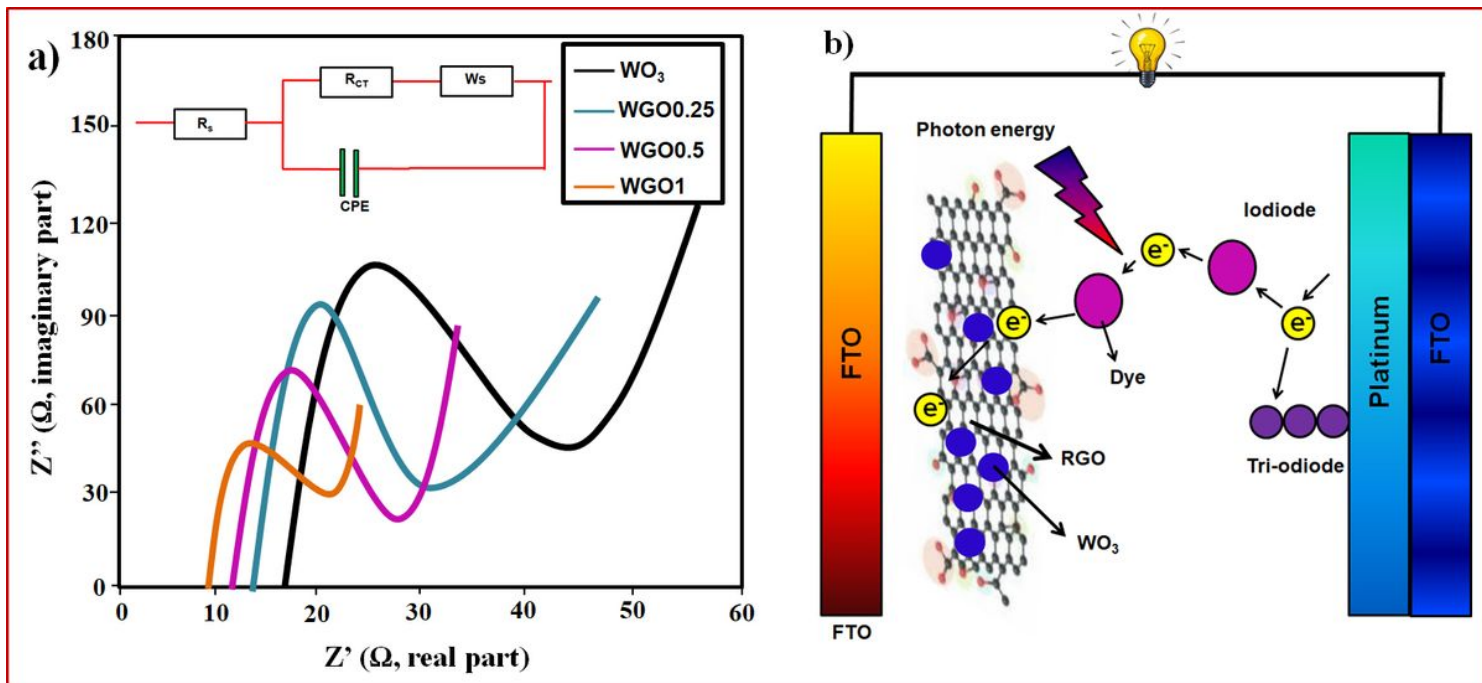


Figure 9

a) Nyquist plot with equivalent circuit; (b) Schematic representation for photovoltaic conversion mechanism of RGO/ WO_3

Supplementary Files

This is a list of supplementary files associated with this preprint. Click to download.

- [Table1.jpg](#)
- [Table2.jpg](#)